Research Article Vol. 10, No. 8 / August 2022 / Photonics Research 1819

PHOTONICS Research

Tunable mechanical-mode coupling based on nanobeam-double optomechanical cavities

Qiancheng Xu,[1,2] Kaiyu Cui,[1,2,*] Ning Wu,[1,2] Xue Feng,[1,2] Fang Liu,[1,2] Wei Zhang,[1,2,3] and Yidong Huang[1,2,3]

[1]Department of Electronic Engineering, Tsinghua University, Beijing 100084, China
[2]Beijing National Research Center for Information Science and Technology (BNRist), Tsinghua University, Beijing 100084, China
[3]Beijing Academy of Quantum Information Sciences, Beijing, China
*Corresponding author: kaiyucui@tsinghua.edu.cn

Received 10 November 2021; revised 18 April 2022; accepted 2 June 2022; posted 3 June 2022 (Doc. ID 447711); published 19 July 2022

Tunable coupled mechanical resonators with nonequilibrium dynamic phenomena have attracted considerable attention in quantum simulations, quantum computations, and non-Hermitian systems. In this study, we propose tunable mechanical-mode coupling based on nanobeam-double optomechanical cavities. The excited optical mode interacts with both symmetric and antisymmetric mechanical supermodes and mediates coupling at a frequency of approximately 4.96 GHz. The mechanical-mode coupling is tuned through both optical spring and gain effects, and the reduced coupled frequency difference in non-Hermitian parameter space is observed. These results benefit research on the microscopic mechanical parity–time symmetry for topology and on-chip high-sensitivity sensors.

https://doi.org/10.1364/PRJ.447711

1. INTRODUCTION

Mechanical resonators exhibiting nanomechanical or micromechanical motion with long-lifetime vibrational phonon modes have been studied extensively for classical and quantum information processing. Multi-mechanical resonators are used in applications such as ultrasensitive sensing [1,2], macroscopic quantum entanglement [3,4], dual-mode squeezing [5,6], coherent Rabi oscillation [7], synchronization [8,9], and information processing [10–12]. Therefore, some chip-based coupled mechanical resonators, including microdisk cavities [8,13], silicon nitride membranes [14], carbon nanotubes [7], graphene [15], and photonic crystals [12,13], have been reported to develop integrated hybrid quantum systems [16–18].

With these advances, tunable coupled mechanical resonators have attracted considerable attention because these resonators are used to investigate nonequilibrium dynamic phenomena in quantum simulation [19–21], minimize decoherence errors caused by unwanted interactions in quantum computation [22–24], and determine exceptional points (EPs) in non-Hermitian systems [14,25,26]. In coupled mechanical resonators, system parameters including frequency, coupling rate, and dissipation can be controlled by applying the electrostatic field [27], piezoelectric actuator [28], or cavity optomechanical (OM) interaction [13]. Among these techniques, cavity optomechanics, which describes nonlinear interaction between the light and mechanical modes in the same resonator, has been developed rapidly [7–15], and coherent mixing in a tunable zipper cavity and double-disk cavity with frequency approximately 10 MHz has been demonstrated [13]. However, some important applications need higher mechanical frequencies with larger tunability, such as quantum information processing [3,4,29,30], where a critical prerequisite is requiring mechanical resonators with frequencies beyond the GHz range for mechanical quantum ground states in the resolve sideband regime (mechanical resonant frequency larger than the optical dissipation rate) [29–31]. Tunable coupled mechanical resonators with high mechanical frequency have great potential for realizing high-sensitivity EPs sensors with an increased resistance to environmental disturbances and sensing bandwidth [32,33], and investigating non-Hermitian systems with multi-physics scenarios [14,25,26]. Therefore, the realization of coupled mechanical resonators with both high frequency and large tunability is crucial for quantum information and non-Hermitian systems.

In this study, we propose the manipulation of mechanical-mode coupling beyond GHz range based on nanobeam-double OM cavities (OMCs) by using optical spring and optical gain effects. The optical spring effect was used to change the mechanical-mode frequency to realize mode degeneracy of two mechanical resonators. Furthermore, the optical gain effect was exploited to manipulate mechanical coupling by adjusting mechanical loss. The influence of the mechanical coupling interaction was analyzed using coupled-mode theory. In experiments, mechanical-mode coupling between two mechanical supermodes of the proposed structure with a frequency of

approximately 4.96 GHz was realized through asymmetric tapered fiber coupling. The frequency difference of the two mechanical supermodes can be dynamically controlled by changing the power and wavelength of the pump laser. This result can provide a guideline for achieving microscopic mechanical parity–time symmetry to realize topology [14] and high-sensitivity sensor chips [34,35].

2. CAVITY STRUCTURES AND MECHANICAL-MODE COUPLING

In the nanobeam-double OMCs studied here, two identical nanobeam OMCs are connected along the nanobeam length direction to form side-coupled cascaded cavities, as displayed in Figs. 1(a) and 1(b). The single OMC is designed based on our previous work [36]. The period of the unit cell is 380 nm, and the width of nanobeam is 500 nm. The radius of the air hole in the mirror cell is 105 nm, and the radius of the air hole in the defect cell is 125.5 nm. Three mechanical modes with frequencies of 4.96 GHz (fundamental mode), 5.14 GHz (second mode), and 5.28 GHz (third mode) are obtained by the finite element method and their OM coupling rates ($g_0/2\pi$) with the same optical mode are 0.57, 0.65, and 0.28 MHz, respectively.

The two single OMCs are coupled through energy exchange in the center mirror region between the two cavities, leading to the emergence of mechanical supermodes. For the mechanical fundamental modes, two supermodes are categorized into the symmetric supermode (SSM) and antisymmetric supermode (ASM). The former is the mechanical modes in the two single OMCs vibrating in the same direction, and the latter is that vibrating in the opposite direction, as illustrated in Fig. 1(c). The frequency difference caused by the mode splitting between SSM and ASM reflects the mechanical coupling rate. For the proposed nanobeam-double OMCs, the mechanical coupling rate is determined by the design of the center mirror between the two cavities. The calculated mechanical coupling rate changes with the quantity and the radius of the center mirror cell, as presented in Fig. 1(e). A low mechanical coupling rate contributed considerably to the mechanical-mode coupling change monitored by the OM interaction in our system and is an essential factor in observing parity–time symmetry and sensing application. Therefore, the mechanical coupling rate is designed to approximately 1 MHz to satisfy the weak coupling condition.

When the tapered fiber is set near one end of the nanobeam [Fig. 1(a)], the symmetric distribution of the refractive index for the two optical cavities in the nanobeam structure is broken. Thus, the optical field is localized in one cavity (detailed simulation can be seen in Appendix A), as displayed in Fig. 1(d). This type of optical mode design has one advantage in that the excited optical mode can interact with both mechanical SSM and ASM.

For the proposed OMCs as a dissipative system, mechanical coupling interaction is determined not only by the mechanical coupling rate but also by the mechanical loss because the mechanical energy exchange process is influenced by various lifetimes of mechanical modes, corresponding to mechanical loss. Based on this principle, we used the optical damping (gain for blue-detuned pump) effect [37,38] to change the mechanical loss in OM interaction to control the mechanical coupling process. This process can be described by the following mechanical coupling equation:

$$\begin{aligned} &\ddot{x}_1 + (\Gamma_m + \Gamma_{\text{opt}})\dot{x}_1 + (\Omega_m + \delta\Omega_m)^2 x_1 + \Omega_m k x_2 = F_1/m_{\text{eff}}, \\ &\ddot{x}_2 + \Gamma_m \dot{x}_2 + \Omega_m^2 x_2 + \Omega_m k x_1 = F_2/m_{\text{eff}}, \end{aligned} \tag{1}$$

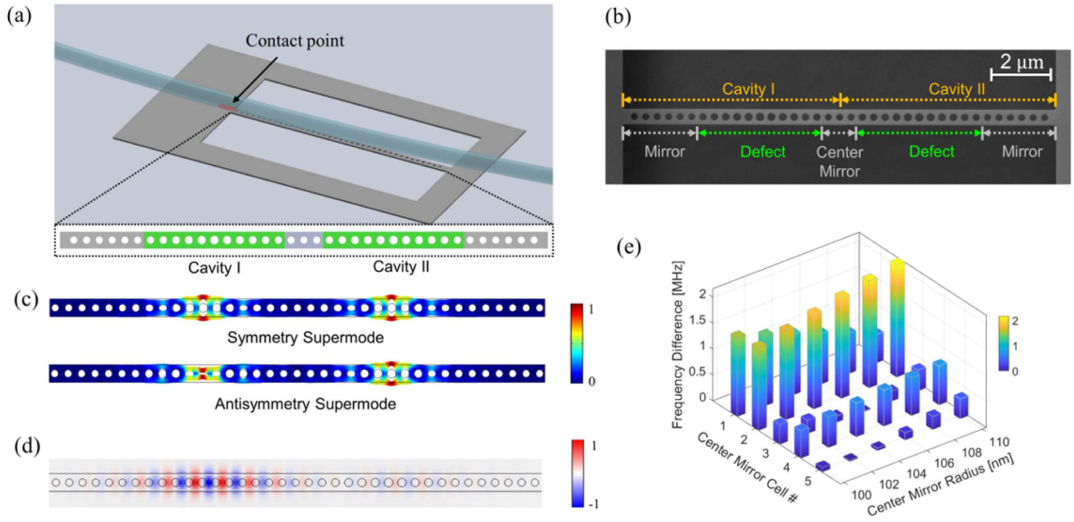

Fig. 1. Nanobeam-double optomechanical cavities (OMCs). (a) Schematic of asymmetric photonic coupling of a tapered fiber contacting one end of the nanobeam-double OMCs. The distances between the tapered fiber and the two original single cavities are different, which breaks the symmetric refractive index distribution and leads to only one excited optical mode of the double cavities in (d). The inset image presents a schematic of the nanobeam-double OMCs. The green parts are cavity defect regions formed by gradually varied hole radius. The gray parts are cavity mirrors for both optical and mechanical modes. (b) Top-view scanning electron microscope (SEM) micrograph of the nanobeam-double OMCs. (c) Normalized displacement of the mechanical symmetric supermode (SSM) and antisymmetric supermode (ASM). (d) Normalized E_y of the excited optical mode by the asymmetric photonic coupling fiber. (e) Mechanical cavity coupling rate with center mirror cell quantity and center mirror radius.

where x_1 and x_2 are displacements of the mechanical single cavity mode, κ is the mechanical coupling rate, m_{eff} is the effective mass of the mechanical mode, and F_1 and F_2 are fluctuating forces. To simplify the physical model, mechanical frequency Ω_m and intrinsic loss Γ_m of the two modes were set to be equal. Furthermore, Γ_{opt} is the optical damping rate, and $\delta\Omega_m$ is the optical spring detuning because of OM interaction. Unlike the mechanical coupling rate, the optical damping rate and optical spring detuning were not fixed, which depended on the pump power and pump wavelength of light. The optical damping rate was considerably greater than the intrinsic mechanical loss, which provided a large-scale mechanical loss control at a high pump power [39]. Because we used blue-detuned pump light, the OM interaction generated gain instead of loss contributed to the mechanical-mode coupling change in our experiments (detailed discussions are presented in Appendix B).

3. EXPERIMENTS FOR ACHIEVING TUNABLE MECHANICAL-MODE COUPLING

In this experiment, the patterns of the designed structures were defined by using electron beam lithography (EBL), and then these patterns were transferred to the device layer of silicon-on-insulator (SOI) chips using inductively coupled plasma (ICP) etching. Afterward, buffered hydrofluoric (BHF) acid was used to remove the buried oxide layer and form suspended structures.

After the fabrication process, we measured the mechanical coupling of the fabricated nanobeam-double OMCs by using the experimental setup in Fig. 2(a). The optical modes of the nanobeam-double OMCs were detected by using a tapered fiber on one end of the nanobeam. According to the Lorentz fitting of the spectrum at −20 dBm of pump power [Fig. 2(b)], the intrinsic optical Q factor for the fabricated cavity was 86,000. The mechanical spectrum information was obtained by analyzing the power spectral density (PSD) of the output light transmission. Figure 2(c) displays the PSD results at a pump power of 0 dBm. The mechanical fundamental mode and two high-order modes are observed in the spectrum. Inside the resonance peak of the fundamental mode, two mechanical modes were obtained for the two mechanical-mode couplings, as displayed in the inset of Fig. 2(c), which is the enlarged image of the fundamental mode. By placing the tapered fiber on the other end of nanobeam, the previous two peaks were still observed, which proved the mechanical-mode coupling between two cavities (see Appendix A for details).

We measured the OM tuning of the nanobeam-double OMCs by changing the pump light power and wavelength. Figure 3(a) displays the coupling process of the two mechanical modes by changing the pump wavelength. The difference in two resonance peaks representing mechanical eigen frequencies at the beginning decreases and then increases when the pump laser wavelength shifts toward red. This result can be explained by the OM gain effect (theoretical details are shown in Appendix B). By fitting the power spectrum of the two coupled mechanical resonators, we plotted the non-Hermitian parameter space diagram of two mechanical-mode eigen frequencies for various pump powers and wavelengths. The smallest mechanical eigen frequency difference decreased from 2.0 MHz at a pump power of 0 dBm to 1.0 MHz at a pump power of 5 dBm. This result revealed that the frequency difference of the symmetric and antisymmetric mechanical mode was tuned to diminish in the parameter space. This phenomenon can provide guidance for obtaining microscopic mechanical parity–time symmetry (see Appendix B for details) for topology [14] and on-chip high-sensitivity sensors [34,35].

4. DISCUSSION ON THE THERMAL EFFECT

We observed the OM interaction and thermal nonlinear effect [40] simultaneously with the increase in pump power. The thermal effect [41] is a common phenomenon in high-Q optical cavities caused by dielectric absorption. In the low-power regime for the driving laser, the optical resonance frequency

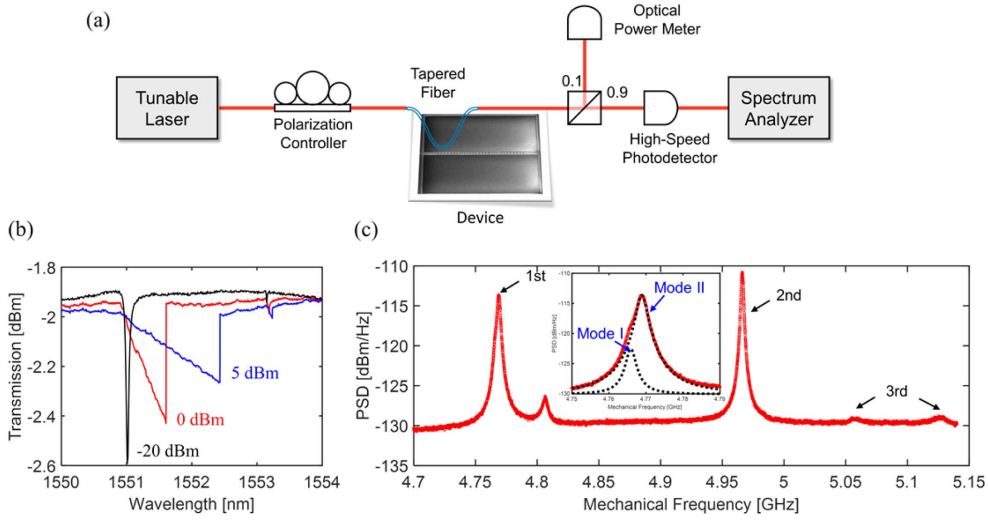

Fig. 2. Experimental setup and optical and mechanical results. (a) Schematic of the experimental setup for mechanical and optical measurement. (b) Optical transmission spectrum with laser power of −20, 0, and 5 dBm. (c) Power spectral density (PSD) for the three types of mechanical modes observed in the spectrum analyzer. The inset displays the detailed PSD of the fundamental modes. The dotted lines are the fitting results reflecting two mechanical-mode couplings.

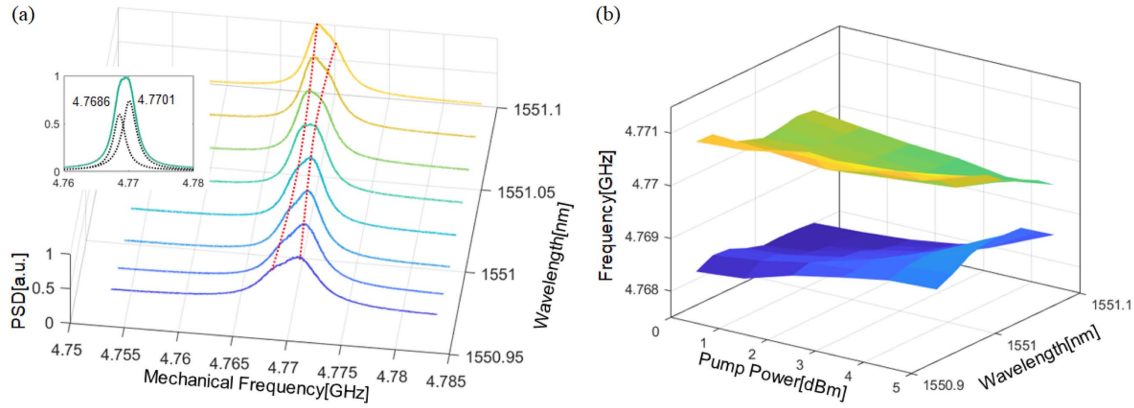

Fig. 3. Optical control of the two mechanical-mode couplings. (a) Normalized mechanical power spectrum density for various pump wavelengths. The red dashed lines reveal the resonance frequencies of two coupled modes. The inset presents an enlarged view of the mechanical spectrum at laser wavelength of 1551.04 nm with the two-component fits. (b) The non-Hermitian parameter space diagram of mechanical-mode coupling with pump power and pump wavelength. The blue and yellow sheets each represent a mechanical mode.

depends on the laser wavelength, as displayed in the asymmetric transmission spectrum in Fig. 2(b). When the laser power exceeded a critical point, the system operated in a bistable region in which the optical energy in the cavity exhibited two possibilities determined by the driving process. The influence of the thermal bistable phenomenon on OM interaction was circumvented by adiabatically tuning the pump wavelength and power. However, the operation becomes complex when the pump power increases further. The thermal effect enhanced the driving of the bistable region to the self-oscillation region. In this case, the optical energy in the cavity oscillated with a frequency of approximately 20 MHz. The oscillations were determined by material properties and structure geometry (a detailed discussion is given in Appendix C). As the optical energy affects the OM interaction, in the self-oscillation region, the OM interaction and thermal nonlinear effect mixed and determined the complete dynamical characteristic of the system. In the mechanical power spectrum, multi-peaks appeared at approximately the mechanical-mode resonance frequencies when the system was driven across the border of the self-oscillation region [Fig. 4(a)]. These peak signals were caused by the thermal nonlinear effect and moved in the frequency domain with the variation in laser wavelength. Near the border of the self-oscillation region, the mechanical signals decreased rapidly, which revealed that OM interaction decreased. This phenomenon can be qualitatively explained as follows: in a thermal self-oscillation period, averaged optical energy in the cavity was less than that in the steady state. Although OM interaction was affected by the thermal nonlinear effect, the two coupled mechanical modes were distinguished by the asymmetric resonance peak in the frequency spectrum near the mechanical mode, as displayed in Fig. 4(b). In this case, the mechanical couplings in the stable and self-oscillation regions are denoted with black and red lines, respectively.

5. CONCLUSION

In this study, we realized tunable mechanical-mode coupling by using nanobeam-double OMCs. The mechanical coupling process can be controlled with the OM gain inside the optically pumped cavity by breaking the optical spatial symmetry in the proposed structure. The frequency difference of the SSM and ASM was tuned to diminish from 2.0 to 1.0 MHz by changing the power and wavelength of the pump laser in experiment and

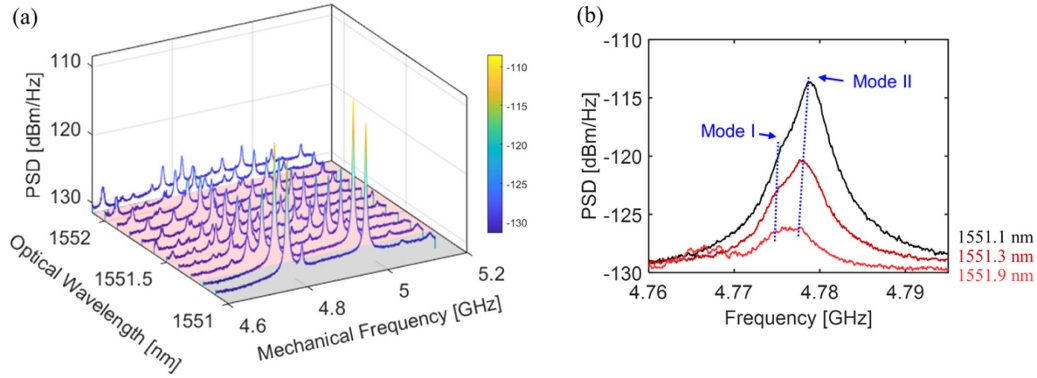

Fig. 4. (a) Thermal oscillation PSD of the nanobeam-double OMCs for various optical wavelengths. The gray and pink regions refer to the thermal stable state and thermal self-oscillation, respectively. (b) Mechanical-mode coupling in the stable region (black line) and self-oscillation region (red lines). The blue dashed lines indicate two mechanical modes.

was further limited by the opto-thermal self-sustained oscillation phenomenon. The tuning of the mechanical-mode coupling based on our demonstrated double OMCs can be used in parity–time symmetry, quantum information, high-sensitivity EP sensing, and mechanical synchronization.

APPENDIX A: ASYMMETRIC OPTICAL COUPLING WITH A TAPERED FIBER SETTING ASIDE

We simulated the optical eigen mode of nanobeam-double OMCs by using a bent fiber. The fiber is parallel with the nanobeam, and the lowest point of the fiber touches one end of the nanobeam, as displayed in Fig. 1. Thus, the tapered fiber setting breaks the optical spatial symmetry of the double cavities, and only one of the nanobeam-double OMCs can be optically excited.

In our simulation, the radius of the fiber was set to 0.5 μm, and the bending radius was set to 250 μm. Figure 5 displays the simulation results. The two optical resonance frequencies redshifted 1.6 and 6.8 nm when the fiber contact point was close to the cavity. The optical modes of the two optical cavities changed with the fiber contact position, as displayed in Fig. 5(a). To quantitatively determine the influence of fiber coupling, we defined "optical mode isolation" as the ratio of the optical field energy in one cavity to the other cavity, as presented in Fig. 5(b). An isolation of more than 15 dB can be obtained by using asymmetric fiber coupling, which satisfies the requirement of only one excited optical mode for optical manipulation of mechanical-mode coupling. In our practical measurement, the isolation is estimated as 10 dB from the depth of two optical resonant peaks in the transmission spectrum shown in Fig. 2(b). It indicates that the influence of optical mode coupling through the waveguide can be ignored. Thus, the two mechanical peaks [Figs. 2(c) and 3(a)] do not result from optical coupling, and these two modes are coupled via the mechanical connection.

In the experiment, the optical fiber was set on both ends of the nanobeam to confirm mode coupling between the two resonators. Figure 6 displays the results of this experiment. In both cases, at approximately 4.77 GHz, the existence of two superposed asymmetric resonance peaks revealed that the mechanical modes were coupled.

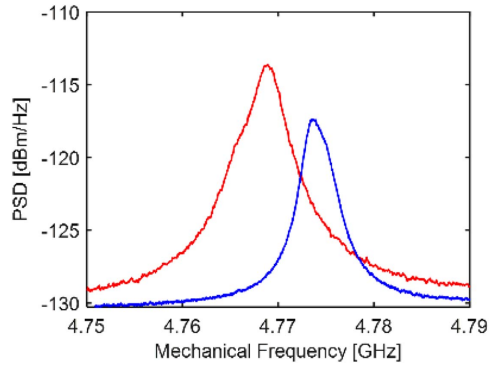

Fig. 6. Superposed asymmetric mechanical modes of the nanobeam-double OMCs. The two curves are the experimental results of the power spectral density (PSD) for the optical fiber on the various ends of the nanobeam.

APPENDIX B: MECHANICAL-MODE COUPLING THEORY

We derived the expressions describing the tuning OM coupling. We started from the classical equations of motion for the light amplitude (a) and the displacements ($x_{1,2}$):

$$\begin{aligned}\dot{a} &= \left(i\Delta - \frac{\gamma_o}{2}\right)a + iGx_1a + \sqrt{\gamma_{oc}}s_{in},\\ \ddot{x}_1 &= -\Omega_m^2 x_1 - \Gamma_m\dot{x}_1 - \Omega_m\kappa x_2 + \hbar G|a|^2/m_{eff} + F_1/m_{eff},\\ \ddot{x}_2 &= -\Omega_m^2 x_2 - \Gamma_m\dot{x}_2 - \Omega_m\kappa x_1 + F_2/m_{eff},\end{aligned} \tag{B1}$$

where $\Delta = \omega_l - \omega_o$ is the optical frequency in a frame rotating at pumping frequency ω_l, and γ_o is the optical decay rate composed of intrinsic loss γ_i and waveguide coupling rate γ_{oc}. Parameter s_{in} is the pumping light at the input of the cavity. Furthermore, m_{eff}, Ω_m, and Γ_m are mechanical effective mass, frequency, and loss, respectively; G is the linear OM coupling rate describing optical frequency shift per displacement; κ is the mechanical coupling rate; and $F_{1,2}$ are fluctuating forces. As the laser power is lower than the mechanical lasing threshold, linearization approximation ($a \to \bar{a} + a$, $x_{1,2} \to \bar{x}_{1,2} + x_{1,2}$) is sufficient to describe our system. Therefore, we obtained the following expression:

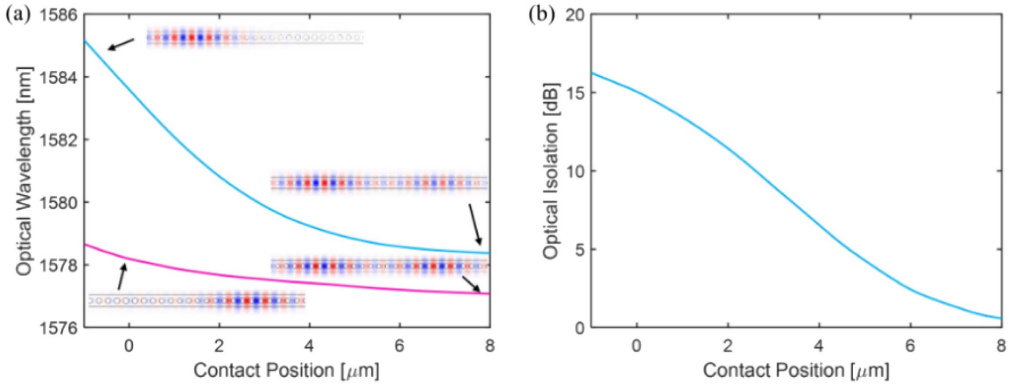

Fig. 5. (a) Optical resonance wavelengths and (b) optical mode isolation as a function of the contact position along the length direction of the nanobeam-double OMCs. The insets in (a) illustrate the normalized electric y component of the optical modes of the two optical cavities.

$$\dot{a} = \left(i\tilde{\Delta} - \frac{\gamma_o}{2}\right)a + iG\tilde{a}x_1,$$
$$\ddot{x}_1 = -\Omega_m^2 x_1 - \Gamma_m \dot{x}_1 - \Omega_m \kappa x_2 + \hbar G(\tilde{a}^* a + \tilde{a} a^*)/m_{\text{eff}} + F_1/m_{\text{eff}},$$
$$\ddot{x}_2 = -\Omega_m^2 x_2 - \Gamma_m \dot{x}_2 - \Omega_m \kappa x_1 + F_2/m_{\text{eff}}, \quad \textbf{(B2)}$$

$$\tilde{a} = \frac{\sqrt{\gamma_{\text{oc}}}s_{\text{in}}}{-i\tilde{\Delta} + \gamma_o/2},$$
$$\tilde{x}_1 = \frac{\hbar G\tilde{a}^2}{m_{\text{eff}}(\Omega_m^2 - \kappa^2)},$$
$$\tilde{x}_2 = -\frac{\kappa}{\Omega_m}\frac{\hbar G\tilde{a}^2}{m_{\text{eff}}(\Omega_m^2 - \kappa^2)}, \quad \textbf{(B3)}$$

where $\tilde{\Delta} = \Delta + G\tilde{x}$ is the corrected detuning. Because the optical decay rate ($\gamma_o/2\pi \sim 6.5$ GHz) is considerably larger than the OM coupling ($G\tilde{a}x_{zpf}/2\pi \sim 0.5$ GHz) in our system, the optical mode can be adiabatically eliminated [42,43]. Therefore, we defined $x_+ = x_1 + x_2$ as displacement of mechanical SSM and $x_- = x_1 - x_2$ as displacement of mechanical ASM. The mechanical equations can be rewritten as follows:

$$\ddot{x}_+ + \left(\Gamma_m + \frac{1}{2}\Gamma_{\text{opt}}\right)\dot{x}_+ + (\Omega_m^2 + \Omega_m\kappa + \Omega_m\delta\Omega_m)x_+ = -\Omega_m\delta\Omega_m x_- - \frac{1}{2}\Gamma_{\text{opt}}\dot{x}_- + F_+/m_{\text{eff}},$$
$$\ddot{x}_- + \left(\Gamma_m + \frac{1}{2}\Gamma_{\text{opt}}\right)\dot{x}_- + (\Omega_m^2 - \Omega_m\kappa + \Omega_m\delta\Omega_m)x_- = -\Omega_m\delta\Omega_m x_+ - \frac{1}{2}\Gamma_{\text{opt}}\dot{x}_+ + F_-/m_{\text{eff}}, \quad \textbf{(B4)}$$

where

$$\delta\Omega_m = \frac{8g^2\Omega_m}{\gamma_o^2 + 16\Omega_m^2},$$
$$\Gamma_{\text{opt}} = -\frac{4g^2}{\gamma_o}\frac{16\Omega_m^2}{\gamma_o^2 + 16\Omega_m^2} \quad \textbf{(B5)}$$

are mechanical frequency shift and OM damping rate when $\tilde{\Delta} = \Omega_m$ (minus sign means gain for blue-detuned pump) [37]. Clearly, the coupling between the SSM and ASM modes is controlled by the laser in the system. Equation (B4) indicates that mechanical SSM and ASM are no longer orthogonal when OM interaction exists. To obtain the steady-state solution, we display the linearized Eq. (B2) in the frequency space as follows:

$$\epsilon^{-1}(\omega)a(\omega) = iG\tilde{a}x_1(\omega),$$
$$\chi_1^{-1}(\omega)x_1(\omega) = -\Omega_m\kappa x_2(\omega) + F_1(\omega)/m_{\text{eff}},$$
$$\chi_2^{-1}(\omega)x_2(\omega) = -\Omega_m\kappa x_1(\omega) + F_2(\omega)/m_{\text{eff}}, \quad \textbf{(B6)}$$

where

$$\epsilon^{-1}(\omega) = -i(\omega + \tilde{\Delta}) + \frac{\gamma_o}{2},$$
$$\chi_1^{-1}(\omega) = \Omega_m^2 - \omega^2 - i\omega\Gamma_m - i\Sigma(\omega),$$
$$\chi_2^{-1}(\omega) = \Omega_m^2 - \omega^2 - i\omega\Gamma_m,$$
$$\Sigma(\omega) = \frac{\hbar G^2|\tilde{a}|^2}{m_{\text{eff}}}[\epsilon(\omega) - \epsilon^*(-\omega)], \quad \textbf{(B7)}$$

where $\epsilon(\omega)$ and $\chi_{1,2}(\omega)$ are optical and two mechanical-mode susceptibilities, respectively. Here, $\Sigma(\omega)$ reflects the influence of OM interaction on mechanical frequency and loss. Equation (B6) reveals that mechanical displacement can be obtained from mechanical fluctuation forces:

$$x_1(\omega) = \frac{F_1/m_{\text{eff}} - \Omega_m\kappa F_2/m_{\text{eff}}\chi_2}{\chi_1^{-1} - \Omega_m^2\kappa^2\chi_2}. \quad \textbf{(B8)}$$

The optical output power can be obtained from input–output theory as follows:

$$I_o = |s_{\text{in}} - \sqrt{\gamma_{\text{oc}}}(\tilde{a} + a)|^2 \approx \bar{I}_o - \sqrt{\gamma_{\text{oc}}}(d_{\text{in}}^* a + d_{\text{in}} a^*), \quad \textbf{(B9)}$$

$$d_{\text{in}} = \left(1 - \frac{\gamma_{\text{oc}}}{-i\Delta + \gamma_o/2}\right)s_{\text{in}}. \quad \textbf{(B10)}$$

By using Eq. (B6), the PSD of the output power signal $S_{\text{II}}(\omega)$, except for a frequency of 0 Hz, can be expressed as follows:

$$S_{\text{II}}(\omega) = |H(\omega)|^2 S_{xx}(\omega), \quad \textbf{(B11)}$$

$$H(\omega) = -i\sqrt{\gamma_{\text{oc}}}G\tilde{a}[d_{\text{in}}^*\epsilon(\omega) - d_{\text{in}}\epsilon^*(-\omega)], \quad \textbf{(B12)}$$

where $S_{xx}(\omega)$ is the PSD of mechanical displacement, and $x_1(\omega)$ and $H(\omega)$ are the transfer functions from mechanical displacement to output power. As the optical susceptibility is slowly varied, transfer function $H(\omega)$ is a constant $H(\Omega_m)$. Therefore, the mechanical motion information can be directly obtained from the PSD of output power:

$$S_{xx}(\omega) = \frac{1 + \Omega_m^2\kappa^2|\chi_2(\omega)|^2}{|\chi_1^{-1}(\omega) - \Omega_m^2\kappa^2\chi_2(\omega)|^2}\frac{S_{\text{FF}}(\omega)}{m_{\text{eff}}^2}. \quad \textbf{(B13)}$$

It is noted that this system shows the potential for demonstrating mechanical parity–time symmetry [43–45]. Here we used $\Omega_m/2\pi = 5$ GHz, $\Gamma_m/2\pi = 3$ MHz, $\gamma_0/2\pi = 5$ GHz, $k/2\pi = 1.25$ MHz, and $\gamma_{\text{oc}}/2\pi = 0.25$ GHz. Thereafter, we calculated the eigenvalues of the mechanical modes, and Fig. 7 demonstrates the difference of the real part of the mechanical eigenvalues. In this simulation, the frequency evolves with these

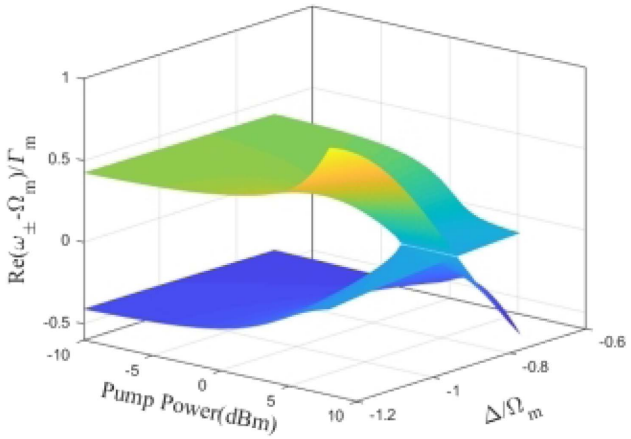

Fig. 7. Calculated non-Hermitian parameter space diagram of normalized mechanical frequency difference with pump power and detuning Δ. The blue and yellow sheets each represent a mechanical mode.

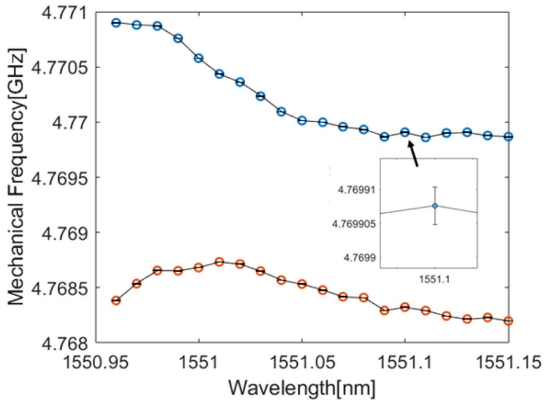

Fig. 8. Mechanical frequency of the corresponding spectra in Fig. 3(a) versus optical wavelength. The orange and blue circles reveal the resonance frequencies of two coupled modes. The inset shows the error bar of the fitted frequency, which is almost negligible.

system parameters (pump power and detuning) and corresponds to the Riemann surface. In addition, the EP appears when the pump power is close to 4 dBm. Figure 8 demonstrates the typical mechanical frequency evolution that corresponds to the experimental spectra in Fig. 3(a). Although the observation of some features of the Riemann sheet, such as the EPs shown in Fig. 7, has been hindered by the self-pulsing effect, we believe that these features can be observed successfully after alleviating the influence of the nonlinear thermal effect in the next step.

APPENDIX C: THERMAL NONLINEARITY

Thermal nonlinearity is the main limitation of optical control because at a high pump power, thermal self-oscillation dominates when the laser wavelength approaches the cavity resonance. Figure 9(a) illustrates the optical transmission at a pump power of 5 dBm in which the cavity resonance is colored by gray and pink, referring to the thermal stable state and thermal self-oscillation, respectively. The thermal stable state region can be categorized into monostability and bistability regions [40], which indicates that the optical cavity energy has two possibilities depending on the initial conditions. In our experiment, we measured the mechanical spectrum density variation by sweeping the laser from the short wavelength to the long wavelength. Only the continuously variable mechanical state was observed during each measurement, which was explained by adiabatic evolution. Therefore, optically controlling the mechanical mode is feasible in the opto-thermal bistability region.

In the thermal self-oscillation region, in addition to thermal nonlinearity, two-photon absorption and free carrier absorption are the other two main nonlinear processes in silicon that can influence the optical control of mechanical modes [46]. The rate equations of optical field amplitude (a), temperature variation (ΔT), and free carrier density (N) are as follows:

$$\begin{aligned}\dot{a}(t) &= \left[i\Delta(t) - \frac{\gamma_o}{2}\right]a(t) + \sqrt{\gamma_c}a_{\text{in}}(t),\\ \Delta\dot{T}(t) &= -\gamma_{\text{th}}\Delta T(t) + \frac{\eta_s}{c_{p,m}}(\gamma_{\text{lin}} + \gamma_{\text{FCA}})|a(t)|^2,\\ \dot{N}(t) &= -\gamma_{\text{fc}}N(t) + \beta_{\text{fc}}|a(t)|^4,\end{aligned} \tag{C1}$$

where the detuning of the input laser frequency from the cavity resonance peak is expressed as follows:

$$\Delta(t) = \omega_l - \omega_o + \omega_o\left[\frac{1}{n}\frac{\mathrm{d}n}{\mathrm{d}T}\Delta T(t) + \frac{1}{n}\frac{\mathrm{d}n}{\mathrm{d}N}N(t)\right]. \tag{C2}$$

The last item represents the cavity resonance frequency variation caused by the thermo-optic and free carrier dispersion effects. In silicon, the thermo-optic effect causes the redshift of the resonance, and the free carrier dispersion effect causes the resonance blueshift, which leads to a competitive relationship. Generally, the thermal decay is much slower than the carrier decay [46,47]. In our device, the thermal decay rate is estimated

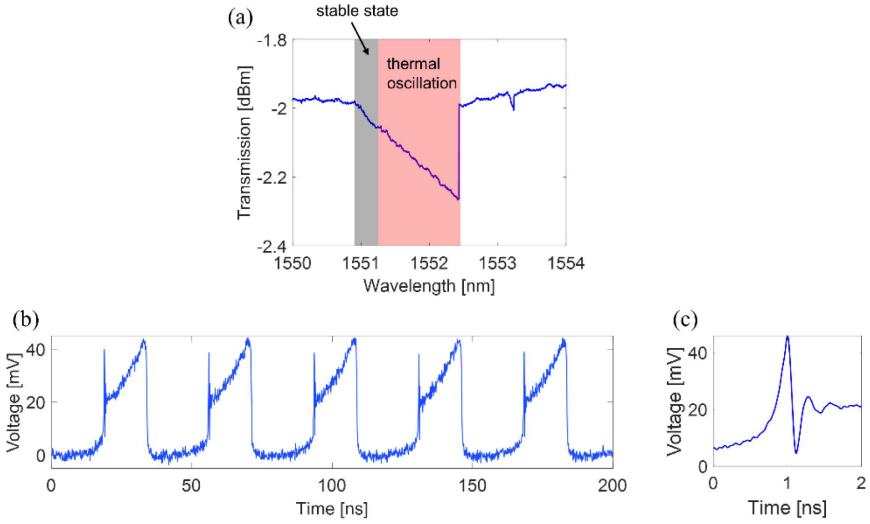

Fig. 9. (a) Optical transmission of the double cavity at a high pump power of 5 dBm. The gray region reveals the optical thermal stable state (including thermal bistability), and the red region denotes the optical thermal self-oscillation. (b) Experimental observation of thermal self-oscillations in a single optomechanical cavity. (c) Details of the pulse front dominated by free carrier dispersion.

to be around 10 MHz since the volume of our OMC is two orders of magnitude smaller than that of the optical microdisk cavity reported in Ref. [46]. Therefore, during the self-oscillation process, cavity resonance was transiently blue detuned by free carriers, causing the cavity resonance to move away from the fixed laser frequency. Subsequently, the thermal effect played a major role in the large redshift until the cavity optical field decreased to zero, and finally, the optical resonance returned to the initial position through thermal relaxation, forming a complete period of motion.

Figure 9(b) displays the time-domain signal of a single-cavity output measured by the oscilloscope in the self-oscillation region. To remove the mechanical motion interferences, we placed the tapered fiber on the center of the cavity to generate a large mechanical vibration damping. The pulse front [Fig. 9(c)] represents the resonance blueshift due to free carrier dispersion, and the thermal effect dominates the remaining time in one pulse period. Figure 9(b) reveals the oscillation period; duty factors are 26.7 MHz and 39.8%, respectively, and both of these parameters can be controlled by the laser power and laser wavelength.

In conclusion, the frequency difference in symmetric and antisymmetric mechanical modes of nanobeam-double OMCs can be tuned by changing the power and wavelength of the pump laser, and the mechanical frequency changing process is affected by the opto-thermal self-sustained oscillation phenomenon at a high pump light power.

Funding. National Key Research and Development Program of China (2018YFB2200402); National Natural Science Foundation of China (61775115, 91750206); Beijing Municipal Natural Science Foundation (Z180012); Beijing Municipal Science and Technology Commission (Z201100004020010); Beijing Frontier Science Center for Quantum Information; Beijing Academy of Quantum Information Sciences.

Acknowledgment. The authors thank Tianjin H-Chip Technology Group Corporation, Innovation Center of Advanced Optoelectronic Chip, and Institute for Electronics and Information Technology in Tianjin, Tsinghua University, for their fabrication support with EBL and ICP etching.

Q.X. designed the structure and conducted the experiments, and Q.X. and K.C. analyzed the experimental results. K.C. and Q.X. conceived the study. K.C. and Y.H. supervised the project. K.C. and Q.X. wrote the paper. N.W., X.F., F.L., W.Z., and Y.H. discussed the results and reviewed the paper.

Disclosures. The authors declare no conflicts of interest.

Data Availability. The data that support the plots within this paper and other findings are available from the corresponding author upon reasonable request.

REFERENCES

1. M. Spletzer, A. Raman, A. Q. Wu, X. Xu, and R. Reifenberger, "Ultrasensitive mass sensing using mode localization in coupled microcantilevers," Appl. Phys. Lett. **88**, 254102 (2006).
2. H. Okamoto, N. Kitajima, K. Onomitsu, R. Kometani, S. Warisawa, S. Ishihara, and H. Yamaguchi, "High-sensitivity charge detection using antisymmetric vibration in coupled micromechanical oscillators," Appl. Phys. Lett. **98**, 014103 (2011).
3. C. F. Ockeloen-Korppi, E. Damskägg, J.-M. Pirkkalainen, M. Asjad, A. A. Clerk, F. Massel, M. J. Woolley, and M. A. Sillanpää, "Stabilized entanglement of massive mechanical oscillators," Nature **556**, 478–482 (2018).
4. R. Riedinger, A. Wallucks, I. Marinković, C. Löschnauer, M. Aspelmeyer, S. Hong, and S. Gröblacher, "Remote quantum entanglement between two micromechanical oscillators," Nature **556**, 473–477 (2018).
5. I. Mahboob, H. Okamoto, K. Onomitsu, and H. Yamaguchi, "Two-mode thermal-noise squeezing in an electromechanical resonator," Phys. Rev. Lett. **113**, 167203 (2014).
6. A. Pontin, M. Bonaldi, A. Borrielli, L. Marconi, F. Marino, G. Pandraud, G. A. Prodi, P. M. Sarro, E. Serra, and F. Marin, "Dynamical two-mode squeezing of thermal fluctuations in a cavity optomechanical system," Phys. Rev. Lett. **116**, 103601 (2016).
7. D. Zhu, X.-H. Wang, W.-C. Kong, G.-W. Deng, J.-T. Wang, H.-O. Li, G. Cao, M. Xiao, K.-L. Jiang, X.-C. Dai, G.-C. Guo, F. Nori, and G.-P. Guo, "Coherent phonon rabi oscillations with a high-frequency carbon nanotube phonon cavity," Nano Lett. **17**, 915–921 (2017).
8. M. Zhang, G. S. Wiederhecker, S. Manipatruni, A. Barnard, P. McEuen, and M. Lipson, "Synchronization of micromechanical oscillators using light," Phys. Rev. Lett. **109**, 233906 (2012).
9. M. Bagheri, M. Poot, L. Fan, F. Marquardt, and H. X. Tang, "Photonic cavity synchronization of nanomechanical oscillators," Phys. Rev. Lett. **111**, 213902 (2013).
10. F. D. Bannon, J. R. Clark, and C. T.-C. Nguyen, "High-Q HF microelectromechanical filters," IEEE J. Solid-State Circuits **35**, 512–526 (2000).
11. R. B. Karabalin, R. Lifshitz, M. C. Cross, M. H. Matheny, S. C. Masmanidis, and M. L. Roukes, "Signal amplification by sensitive control of bifurcation topology," Phys. Rev. Lett. **106**, 094102 (2011).
12. K. Fang, M. H. Matheny, X. Luan, and O. Painter, "Optical transduction and routing of microwave phonons in cavity-optomechanical circuits," Nat. Photonics **10**, 489–496 (2016).
13. Q. Lin, J. Rosenberg, D. Chang, R. Camacho, M. Eichenfield, K. J. Vahala, and O. Painter, "Coherent mixing of mechanical excitations in nano-optomechanical structures," Nat. Photonics **4**, 236–242 (2010).
14. H. Xu, D. Mason, L. Jiang, and J. G. E. Harris, "Topological energy transfer in an optomechanical system with exceptional points," Nature **537**, 80–83 (2016).
15. G. Luo, Z.-Z. Zhang, G.-W. Deng, H.-O. Li, G. Cao, M. Xiao, G.-C. Guo, L. Tian, and G.-P. Guo, "Strong indirect coupling between graphene-based mechanical resonators via a phonon cavity," Nat. Commun. **9**, 383 (2018).
16. Z.-L. Xiang, S. Ashhab, J. Q. You, and F. Nori, "Hybrid quantum circuits: superconducting circuits interacting with other quantum systems," Rev. Mod. Phys. **85**, 623–653 (2013).
17. G. Kurizki, P. Bertet, Y. Kubo, K. Mølmer, D. Petrosyan, P. Rabl, and J. Schmiedmayer, "Quantum technologies with hybrid systems," Proc. Natl. Acad. Sci. USA **112**, 3866–3873 (2015).
18. A. A. Clerk, K. W. Lehnert, P. Bertet, J. R. Petta, and Y. Nakamura, "Hybrid quantum systems with circuit quantum electrodynamics," Nat. Phys. **16**, 257–267 (2020).
19. I. Buluta and F. Nori, "Quantum simulators," Science **326**, 108–111 (2009).
20. A. Polkovnikov, K. Sengupta, A. Silva, and M. Vengalattore, "Colloquium: nonequilibrium dynamics of closed interacting quantum systems," Rev. Mod. Phys. **83**, 863–883 (2011).
21. A. Mezzacapo, L. Lamata, S. Filipp, and E. Solano, "Many-body interactions with tunable-coupling transmon qubits," Phys. Rev. Lett. **113**, 050501 (2014).
22. A. O. Niskanen, K. Harrabi, F. Yoshihara, Y. Nakamura, S. Lloyd, and J. S. Tsai, "Quantum coherent tunable coupling of superconducting qubits," Science **316**, 723–726 (2007).
23. Y. Chen, C. Neill, P. Roushan, N. Leung, M. Fang, R. Barends, J. Kelly, B. Campbell, Z. Chen, B. Chiaro, A. Dunsworth, E. Jeffrey, A. Megrant, J. Y. Mutus, P. J. J. O'Malley, C. M. Quintana, D. Sank, A. Vainsencher,

J. Wenner, T. C. White, M. R. Geller, A. N. Cleland, and J. M. Martinis, "Qubit architecture with high coherence and fast tunable coupling," Phys. Rev. Lett. **113**, 220502 (2014).
24. F. Yan, P. Krantz, Y. Sung, M. Kjaergaard, D. L. Campbell, T. P. Orlando, S. Gustavsson, and W. D. Oliver, "Tunable coupling scheme for implementing high-fidelity two-qubit gates," Phys. Rev. Appl. **10**, 054062 (2018).
25. R. Fleury, D. Sounas, and A. Alù, "An invisible acoustic sensor based on parity-time symmetry," Nat. Commun. **6**, 5905 (2015).
26. C. Shi, M. Dubois, Y. Chen, L. Cheng, H. Ramezani, Y. Wang, and X. Zhang, "Accessing the exceptional points of parity-time symmetric acoustics," Nat. Commun. **7**, 11110 (2016).
27. T. Faust, J. Rieger, M. J. Seitner, J. P. Kotthaus, and E. M. Weig, "Coherent control of a classical nanomechanical two-level system," Nat. Phys. **9**, 485–488 (2013).
28. E. S. Leland and P. K. Wright, "Resonance tuning of piezoelectric vibration energy scavenging generators using compressive axial preload," Smart Mater. Struct. **15**, 1413–1420 (2006).
29. T. A. Palomaki, J. W. Harlow, J. D. Teufel, R. W. Simmonds, and K. W. Lehnert, "Coherent state transfer between itinerant microwave fields and a mechanical oscillator," Nature **495**, 210–214 (2013).
30. A. P. Reed, K. H. Mayer, J. D. Teufel, L. D. Burkhart, W. Pfa, X. Ma, R. J. Schoelkopf, E. Knill, and K. W. Lehnert, "Faithful conversion of propagating quantum information to mechanical motion," Nat. Phys. **13**, 1163–1167 (2017).
31. A. D. O'Connell, M. Hofheinz, M. Ansmann, R. C. Bialczak, M. Lenander, E. Lucero, M. Neeley, D. Sank, H. Wang, M. Weides, J. Wenner, J. M. Martinis, and A. N. Cleland, "Quantum ground state and single-phonon control of a mechanical resonator," Nature **464**, 697–703 (2010).
32. K. Cui, Z. Huang, N. Wu, Q. Xu, F. Pan, J. Xiong, X. Feng, F. Liu, W. Zhang, and Y. Huang, "Phonon lasing in a hetero optomechanical crystal cavity," Photon. Res. **9**, 937–943 (2021).
33. F. Pan, K. Cui, G. Bai, X. Feng, F. Liu, W. Zhang, and Y. Huang, "Radiation-pressure-antidamping enhanced optomechanical spring sensing," ACS Photon. **5**, 4164–4169 (2018).
34. H. Hodaei, A. U. Hassan, S. Wittek, H. Garcia-Gracia, R. El-Ganainy, D. N. Christodoulides, and M. Khajavikhan, "Enhanced sensitivity at higher-order exceptional points," Nature **548**, 187–191 (2017).
35. W. Chen, Ş. Kaya Özdemir, G. Zhao, J. Wiersig, and L. Yang, "Exceptional points enhance sensing in an optical microcavity," Nature **548**, 192–196 (2017).
36. Z. Huang, K. Cui, G. Bai, X. Feng, F. Liu, W. Zhang, and Y. Huang, "High-mechanical-frequency characteristics of optomechanical crystal cavity with coupling waveguide," Sci. Rep. **6**, 34160 (2016).
37. M. Aspelmeyer, T. J. Kippenberg, and F. Marquardt, "Cavity optomechanics," Rev. Mod. Phys. **86**, 1391–1452 (2014).
38. J. Zhang, B. Peng, S. Kim, F. Monifi, X. Jiang, Y. Li, P. Yu, L. Liu, Y. Liu, A. Alù, and L. Yang, "Optomechanical dissipative solitons," Nature **600**, 75–80 (2021).
39. J. Chan, T. P. M. Alegre, A. H. Safavi-Naeini, J. T. Hill, A. Krause, S. Gröblacher, M. Aspelmeyer, and O. Painter, "Laser cooling of a nanomechanical oscillator into its quantum ground state," Nature **478**, 89–92 (2011).
40. T. Carmon, L. Yang, and K. J. Vahala, "Dynamical thermal behavior and thermal self-stability of microcavities," Opt. Express **12**, 4742–4750 (2004).
41. N. Wu, K. Cui, X. Feng, F. Liu, W. Zhang, and Y. Huang, "Hetero-optomechanical crystal zipper cavity for multimode optomechanics," Photonics **9**, 78 (2022).
42. K. Jähne, C. Genes, K. Hammerer, M. Wallquist, E. S. Polzik, and P. Zoller, "Cavity-assisted squeezing of a mechanical oscillator," Phys. Rev. A **79**, 063819 (2009).
43. X. Xu, Y. Liu, C. Sun, and Y. Li, "Mechanical PT symmetry in coupled optomechanical systems," Phys. Rev. A **92**, 013852 (2015).
44. Z. Feng, J. Ma, and X. Sun, "Parity–time-symmetric mechanical systems by the cavity optomechanical effect," Opt. Lett. **43**, 4088–4091 (2018).
45. Ş. K. Özdemir, S. Rotter, F. Nori, and L. Yang, "Parity–time symmetry and exceptional points in photonics," Nat. Mater. **18**, 783–798 (2019).
46. T. J. Johnson, M. Borselli, and O. Painter, "Self-induced optical modulation of the transmission through a high-*Q* silicon microdisk resonator," Opt. Express **14**, 817–831 (2006).
47. D. Woolf, P. Hui, E. Iwase, M. Khan, A. W. Rodriguez, P. Deotare, I. Bulu, S. G. Johnson, F. Capasso, and M. Loncar, "Optomechanical and photothermal interactions in suspended photonic crystal membranes," Opt. Express **21**, 7258–7275 (2013).